ceramics

MDPI

Article

Deriving Principles of the Freeze-Foaming Process by Nondestructive CT Macrostructure Analyses on Hydroxyapatite Foams

Matthias Ahlhelm [1,*], David Werner [1], Nils Kaube [2], Johanna Maier [2], Johannes Abel [1], Thomas Behnisch [2], Tassilo Moritz [1], Alexander Michaelis [1] and Maik Gude [2]

1 Fraunhofer Institute for Ceramic Technologies and Systems, IKTS, Winterbergstraße 28, 01277 Dresden, Germany; david.werner@ikts.fraunhofer.de (D.W.); johannes.abel@ikts.fraunhofer.de (J.A.); tassilo.moritz@ikts.fraunhofer.de (T.M.); alexander.michaelis@ikts.fraunhofer.de (A.M.)

2 Institute of Lightweight Engineering and Polymer Technology, Technische Universität Dresden, Holbeinstr. 3, 01307 Dresden, Germany; nils.kaube@mailbox.tu-dresden.de (N.K.); johanna.maier@tu-dresden.de (J.M.); thomas.behnisch@tu-dresden.de (T.B.); maik.gude@tu-dresden.de (M.G.)

* Correspondence: matthias.ahlhelm@ikts.fraunhofer.de; Tel.: +49-351-2553-7572

Received: 2 May 2018; Accepted: 8 June 2018; Published: 17 June 2018

Abstract: Freeze Foaming is a direct foaming method that aims at manufacturing ceramic cellular scaffolds for diverse applications. Next to porous structures for a potential use as refractories, the focus lies on potential bone replacement material. The main challenge of this foaming method is to achieve a homogeneous and predictable pore morphology. That is why, in a current project, the authors report on the pore morphology formation and evolution of the foaming process by means of nondestructive testing. This contribution primarily compares the effect of the suspension's temperature on the resulting foam structure (foaming at 5 and 40 °C). As a basis for computed tomographic analysis, a stable and reproducible model suspension was developed that resulted in reproducible foam structures. Characterized by viscosity, foam structure analyses and foaming rate, the resulting Freeze Foams became adjustable with regards to their porosity and pore shape/size. Under certain conditions, we succeeded in achieving a relatively homogeneous pore structure, as proven by computed tomography-derived quantitative analysis.

Keywords: Freeze Foaming; bioceramics; foaming process; computed tomography; none destructive testing; cellular ceramics

1. Introduction

1.1. The Freeze-Foaming Process and Recent Achievements

The Freeze-Foaming process can be classified into direct foaming methods in which suspensions are foamed either by turbulent mixing with surfactants [1] or by in situ gas and vapor developing reactions [2,3]. The two other industrially relevant techniques are based on polyurethane (PU) foam replication, i.e., the Replica/Schwartzwalder approach [4], and pore forming substances, e.g., polymeric beads, starch, carbon black, wax or sawdust [5,6]. Polymeric scaffolds and pore formers later need to be burned out in order to achieve the desired porous body. No burnout of organic volatile pore formers and polymer scaffolds is needed with so-called Freeze Foaming, which allows the direct foaming of almost any desired material (diverse ceramics, metals, etc.) as long as it can be prepared as an aqueous suspension. The Freeze-Foaming process is triggered by ambient pressure reduction of an aqueous suspension in a freeze dryer. The applied vacuum initiates an inflation of the suspension medium by rising processing air and water vapor. During this foaming step, only a couple

of seconds long, the Freeze Foam's macroporosity evolves (foam cell development). Further foaming takes place with the aqueous system moving along the vapor–liquid equilibrium line towards the triple point (referring to the p,T-diagram of water). After crossing the triple point, the generated protofoam instantaneously freezes and dries via sublimation [7,8]. This freezing step can result in cryogenic structures (discussed in more detail in [9]) similar to typical freeze cast structures [10,11] and accounts for the microporosity of foamed structures. Therefore, the Freeze Foam's only pore formers are rising bubbles of processing air and water vapor as well as sublimated frozen water. After debindering and sintering, the particularly typical ceramic properties can be achieved.

The manifold possibilities concerning material choice and, up until now, basic opportunities to tune the overall porosity of Freeze Foams, allowed the development of potential insulating refractory bricks made of mullite. It has been shown that, by altering the amount of binder, surfactant, solid content and suspension temperature, a different pore morphology as well as different thermomechanical characteristics can be achieved [12]. The conclusion had been reached that manufacturing refractory bricks by this method is within reach. Although only at a small batch scale, especially near net shaped complex structures (Figure 1) were obtained. Further research has been undertaken concerning the material composition, but adjustment of the optimal pore size is the most crucial variable for sophisticated application.

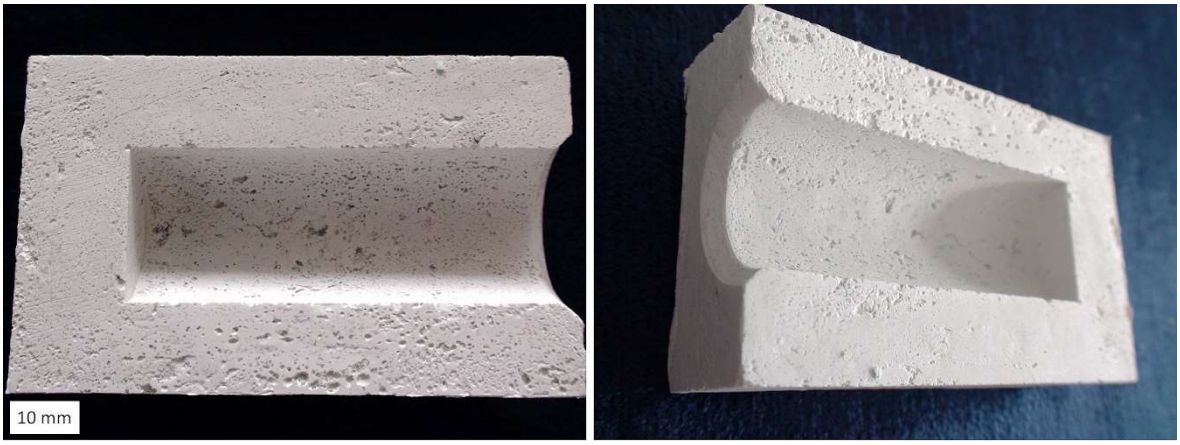

Figure 1. Near net-shaped mullite refractory brick by Freeze Foaming.

The main interest, though, lies in the sector of biomedical technology. With changing the material to bioceramics, the field of synthetic implants and bone replacement material is being addressed. Mainly open porous and interconnected cellular structures have been achieved, which are applicable as biocompatible components when made of hydroxyapatite (HAp), ZrO_2 or a composite mixture [13–15]. Recent research is concerned with a hybrid shaping method: First, three-dimensional, complex-shaped hollow shell geometries are manufactured, for instance by Additive Manufacturing processes. In a second step, those shell structures are filled with a ceramic suspension with the Freeze-Foaming process commenced in situ. That process allows for connecting porous/cellular features provided by the Freeze Foaming with the dense and complex features provided by 3D printing methods like LCM (Lithography-based Ceramic Manufacturing). Bioactive femoral bone model demonstrators and dense-porous segmental components (Figure 2) were successfully co-sintered to one composite part [16,17]. This hybrid shaping technology therefore offers a wide range of application potential for personalized and surface customizable implant structures for application in the field of biomedical technology and engineering.

However, Freeze Foaming and hybrid shaping so far do not exceed the laboratory scale. Upscaling this process requires large batches of reproducible ceramic suspensions. Applications require cellular scaffolds to either have a closed or open as well as often homogeneous pore morphology in order to

provide the targeted properties in a predictable manner. With regard to refractories, homogeneously distributed small pores of typically closed porosity (in the range of 100 nm to 1 mm for proper isolation capability) are required [18]. In contrast, bioceramic scaffolds for bone replacement material require sufficiently large pores (at least 100–500 µm) for cell attachment [19,20], interconnectivity [21] and microporosity [11], as well a general porosity greater than 40% [22–24]. Thus, Freeze Foaming indeed allows for producing open and microporous, as well as interconnected scaffolds. From the example in Figure 2, though, it becomes obvious that cellular Freeze Foams are typically heterogeneous. This makes estimations and assessments of the reproducibility of biocompatibility or mechanical strength very difficult.

Figure 2. Hybrid manufacturing of combined dense-porous segmental components.

Intense basic research into Freeze Foaming's principles with a consideration of the material and processing aspects is needed. A material preparation and process approach must be found that allows for a controlled tuning of the pore morphology and evaluation of pore evolving activities by monitoring the foaming process itself. One solution that allows insights into processes and influence on materials is being provided by computed tomography (CT), which has become a sophisticated tool for improved damage and degradation analyses as well as structural evaluations in the field of material sciences [25–28].

Already detailed in the previous contribution [9], CT analyses were used for the first time to monitor the Freeze-Foaming process and allow for evaluation of foam structuring phenomena. The first results report the successful manufacturing of a model suspension, of reproducible foam structures foamed at room temperature and the dependence of the porosity, pore size and the shape from the pressure reduction rate of the freeze dryer used. In addition, the first indications of a strong influence of the amount of water with regard to the abundance of occurring cryogenic structures were discovered. The task of the related project's next period was to vary the suspension temperature and monitor the tempered suspension's foaming behavior as well as evaluate the resulting pore morphologies. Reproducible ceramic cellular structures were created with 5 °C and 40 °C tempered suspensions. The focus was not on achieving one defined pore size but rather observing and clarifying the phenomena of the Freeze-Foaming process. Since biomaterial application is one of the higher aims, hydroxyapatite was used, which is well known for its similarities to the mineral fraction of bone and its high osteoconductive potential [29–31]. We aimed at reaching a pore size of around 100–700 µm as well as a distribution of pores that was as homogenous as possible. The porosity should be greater than 40% in order to achieve pore morphologic properties that generally meet the requirements for bone replacement material, as stated above. Since only the green state of manufactured Freeze Foams directly reflects the foaming process's effects on the foam structure, the present contribution focuses on green-state ceramic material only. Analyses of the debinded and sintered foams will follow as soon as the results are available.

2. Materials and Methods

Hydroxyapatite (Sigma-Aldrich now Merck KGaA, Darmstadt, Germany; BET = 70.01 m^2/g, d_{50} = 2.64 µm) was chosen as the raw material. The ceramic suspensions consist of water, Dolapix CE 64 (Co. Zschimmer & Schwarz Mohsdorf GmbH & Co. KG, Burgstädt, Germany) as dispersing agent, the ceramic powder, polyvinyl alcohol as binder and a rheological modifier (Tafigel PUR40, Co. Münzing Chemie GmbH, Heilbronn, Germany). The following processing route was conducted: Deionized water was mixed manually with 2 vol % dispersing agent. Subsequently, hydroxyapatite was added (28 vol %), followed by the polyvinyl alcoholic binder (as 13% aqueous solution) and 8 vol % rheological modifier. To pre-mix binder and powder, all components were first stirred manually and afterwards transferred into a centrifugal vacuum mixer (ARV310, Thinky Corporation, Fukuoka, Japan). In order to disperse the particles and reduce agglomeration the mixture was exposed to a high stirring rate (2000 rpm, mixing time 2 × 1 min, with 3 ZrO_2 mixing spheres of 10 mm diameter). Afterwards, the suspensions were filled into specific molds and transferred to the freeze dryer (Lyo Alpha 2-4, LSCplus, Co. Martin Christ Gefriertrocknungsanlagen GmbH, Osterode, Germany) for Freeze Foaming.

For achieving Freeze Foams that have been foamed with a 40 °C tempered suspension, the following sequence was conducted: While mixing the suspension in the vacuum mixer, the foaming molds (cylindrical shape, 14 mm diameter × 20 mm height) were preheated standing in a closed box, which floated in a 45 °C tempered water bath. After suspension preparation, each mold was then filled with the same amount of suspension (2 g) and returned to the preheated and lockable box. After filling (by injection through a die with the same diameter as the cylinder) all rubber molds, they were left in the closed box at 45 °C water temperature for 40 min to eventually reach 40 °C suspension temperature in every mold (measured by a digital thermometer). All molds were then transferred to the freeze dryer and foamed at once. Two thermal elements were used to monitor the suspension temperature throughout the whole foaming process.

For achieving Freeze Foams that have been foamed with a 5 °C tempered suspension, the rubber molds (same as above) were filled with the ceramic suspension and transferred to a freezing chamber (12 min dwelling time at −23 °C) prior to being foamed in the freeze dryer. Again, two thermal elements were used to monitor the suspension temperature throughout the whole foaming process.

All suspensions were characterized by determining the solid content (moisture measurement: MA 100 Sartorius at 110 °C, Sartorius Lab Instruments GmbH & Co. KG, Goettingen, Germany) and viscosity (MCR 302, Anton Paar GmbH, Graz, Austria; plate-plate rotation and housing for controlled heat treatment at 5 and 40 °C).

For microstructure analysis the resulting Freeze Foams were characterized by SEM (Ultra 55, Co. Carl Zeiss, Oberkochen, Germany).

By measuring the height and diameter on three different foam positions of six Freeze Foams each (foamed at 5 and 40 °C) and deriving the average, geometrical porosities were calculated according to:

$$P = 1 - (\rho_{th}/\rho_{bulk}). \quad (1)$$

2.1. CT Evaluation Procedure

The following CT-derived results and statements to homogeneity mainly refer to the macropores (>50 µm) of Freeze Foams, its foam cells, which are the result of rising air and water vapor. Four green-state foams each obtained from 5 °C and 40 °C tempered suspensions were analyzed. Due to resolution restrictions, the apparent micropores are not part of the CT evaluation and rather are detailed in the SEM images. In this subsection we explain how to progress from the reconstructed CT volume to the defect analysis resulting in porosity and level of interconnection (see results in Section 3.2), followed by the foam structure analysis resulting in pore size and strut thicknesses distribution and directional variability of the foam cell volume (see results in Section 3.2.3).

For CT a FCTS 160—IS (Fa. FineTec FineFocus Technologies GmbH, Garbsen, Germany) was used, located at the TUD-ILK, Dresden, Germany. The allocation of three-dimensional (3D) volumetric pore morphology information was managed by using VGStudio Max v3.0 (Volume Graphics GmbH, Heidelberg, Germany [32]) allowing access to volume-based data like porosity, pore size distribution and visualization of the foam volume. The CT measurements were performed with the parameters given in Table 1.

Table 1. Parameters for CT measurements.

Tube Voltage	Tube Current	Detector	Voxel Size	Focus Size
40 kV	180 µA	Flat panel detector	11.7 µm	4 µm

Using VGStudio Max, we quantified pore morphology data of scanned foams (Figure 3, top left) as also detailed in [9]: First a three-dimensional "Region of Interest" (ROI) is defined and the surface determined by automatic software-assisted grey value analyses (definition of pores, material and material surface; Figure 3, top right). A subsequent defect analysis shows the identified foam cells marked in yellow (Figure 3, bottom left). By multiplying the number of voxels with the grey value belonging to air by the volume of a single voxel, the total volume of defects (V_{def}) and the volume of every single identified defect are obtained. Hence, the obtained porosity can be defined as the ratio of V_{def} to the volume of the ROI (V_{ROI}). The level of interconnection among foam cells is represented by the ratio of maximum defect volume V_{max} and volume V_{ROI} [25].

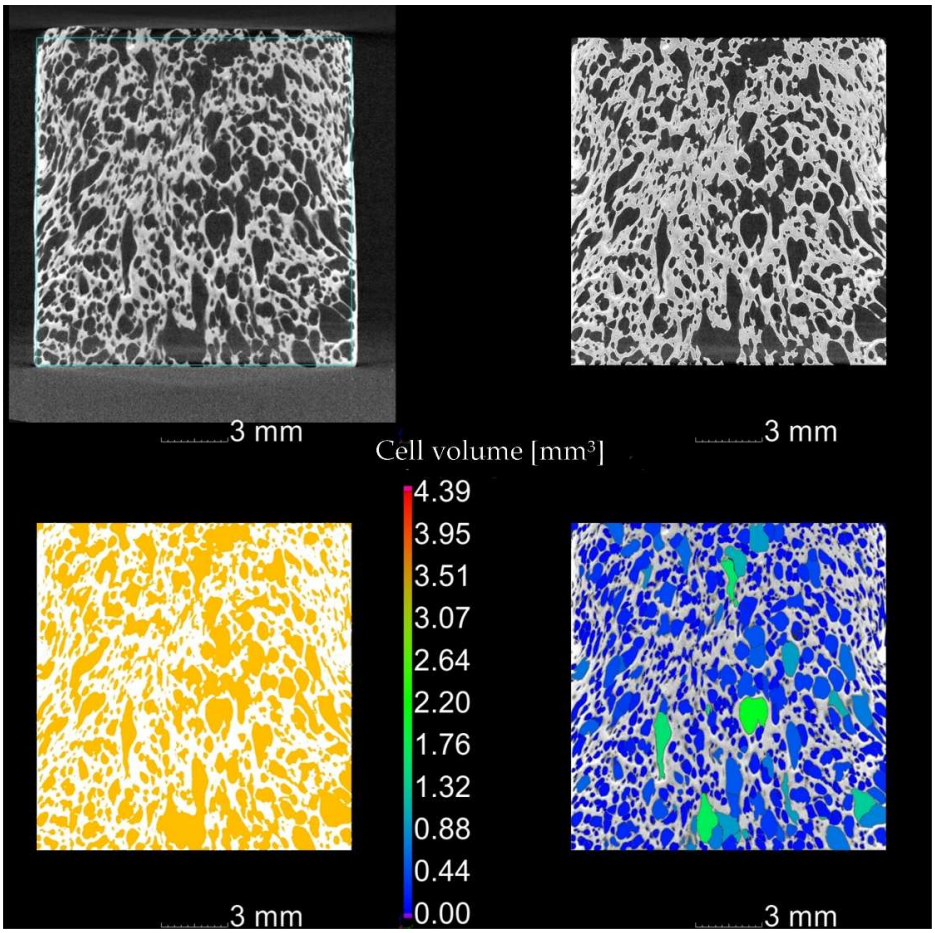

Figure 3. Foam structure analysis procedure on the example of a 5 °C foamed Freeze Foam.

As a last step, the foam structure analysis module is used to separate foam cells that are connected by a cell window (Figure 3, bottom right). A high cell volume corresponds to red and a low volume to blue.

Foam structure analysis requires a segmentation threshold. Its determination was carried out as accurately as possible (adjusted so that small pores remain visible and larger pores are not segmented into smaller ones). That allows for first determining the distribution of strut thicknesses and, secondly, the pore size distribution of manufactured Freeze Foams by transforming the resulting foam cell volume V_{fc} to the equivalent diameter d by the equation:

$$d = (6V_{fc}/\pi)^{1/3}. \quad (2)$$

2.1.1. Quantifying Foam Homogeneity

VGStudio Max 3.0 offers an analysis of the directional variability of foam cell volume. That allows us to gain direction-dependent spatial information about the foam cell size—from bottom to top (i.e., in the foaming direction) and from left to right (perpendicular to the foaming direction). Hence, both directions together provide information about the homogeneity of the foam volume.

With this data we carried out a trend analysis by slicing the foam volume into planes perpendicular to the corresponding analysis direction (in the foaming direction or perpendicular to the foaming direction) with a distance of 0.02 mm from each other. The volume (3D) of all foam cells that lie in the corresponding plane (e.g., z) is averaged ($V_{fc}(z)$).

We furthermore calculated a parameter for the homogeneity of a Freeze Foam's pore morphology by considering the progression of V_{fc} as the profile of the foam's pore morphology—specifically, the cell volume—analogously to the roughness of a surface. According to DIN EN ISO 4287 [33], the following steps are executed: First, we determine the midline of the considered pore morphology profile $V_{fc}(z)$.

With the help of Equation (3)—(Figure 4, solid line)

$$V_{fc0} = V_{fc} - ({V_{fc}}^{min} + {V_{fc}}^{max})/2 \quad (3)$$

—$V_{fc}(z)$ is transferred to the actual profile $V_{fc0}(z)$. This allows us to calculate the arithmetic average V_{fca} of the profile ordinate V_{fc0} as a parameter for the homogeneity of Freeze Foams by deriving the absolute value $|V_{fc0}(z)|$ (Figure 4, dotted line) and integrating to:

$$V_{fca} = 1/h \int_0^h |V_{fc0}(z)| \, dz. \quad (4)$$

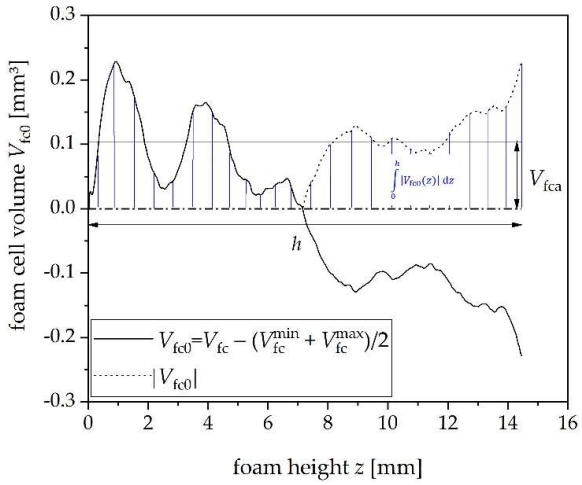

Figure 4. Graph of the arithmetical foam cell's volume average of the profile ordinate.

A high V_{fca} corresponds to a large variability in foam cell volume and, hence, stands for a heterogeneous foam structure. In contrast, a low V_{fca} corresponds to a more homogeneous pore morphology.

3. Results and Discussion

3.1. Reproducibility of Freeze Foams

According to the procedure depicted in Section 2, suspensions were prepared, tempered and characterized. The following graph (Figure 5) illustrates the viscosity curves of 5 and 40 °C tempered suspensions (measured with three suspensions each). As expected, the curve at 5 °C progresses above the 40 °C curve.

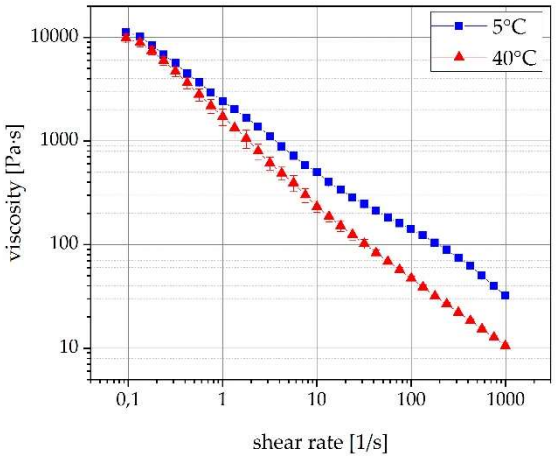

Figure 5. Viscosity of HAp suspensions at 5 and 40 °C (double logarithmic).

Those suspensions were then used for Freeze Foaming. As a result, we were able to achieve a series of reproducible Freeze Foams foamed at 5 °C and 40 °C, proven by measurements of solid content and geometrical porosity (Table 2).

Table 2. Reproducibility of suspensions and Freeze Foams (green state). [1]

Suspension's Temperature (°C)	Solid Content (wt %)	Geometrical Porosity (%)
5	62.7 (SD = 0.7)	81.1 (SD = 0.9)
40	63.4 (SD = 0.4)	79.9 (SD = 1.2)

[1] Five suspensions, six Freeze Foams each; SD = standard deviation.

In order to quantify the actual foaming, we introduce the foaming degree f as the quotient from suspension/foam volume at a specific pressure/time $V_S(t)$ divided by the volume V_0 at the beginning:

$$f(t) = V_S(t)/V_0. \quad (5)$$

Furthermore, we determined the foaming rate (time derivative of $f(t)$). Both parameters are illustrated in Figure 6. For measurements, test glasses were filled with approximately 2 mL suspension tempered at 5 and 40 °C. Both tempered suspensions were then freeze-foamed in the freeze dryer. The ambient pressure in the freeze dryer was lowered in specific pressure steps and the according volume $V_s(t)$ read from the test glasses followed by calculation of $f(t)$ by Equation (5). Table 3 summarizes the pressure values applied during the Freeze-Foaming process for both tempered suspensions and allows us to evaluate the individual foaming behavior (e.g., maximum foaming rate).

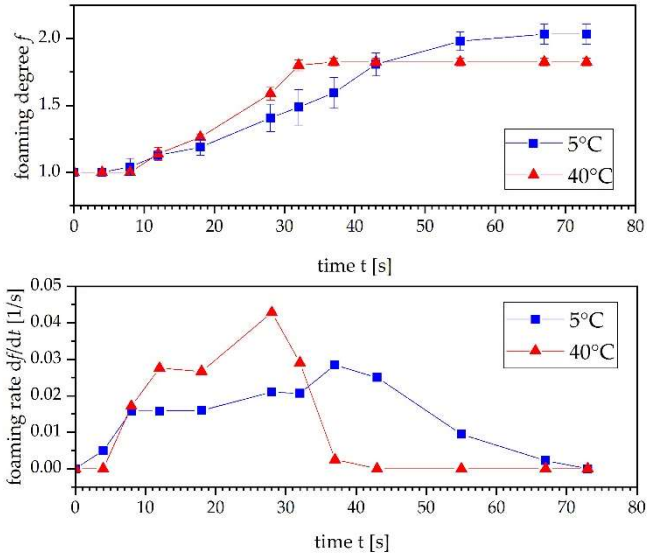

Figure 6. Foaming degree and rate of the Freeze-Foaming process with 5 and 40 °C tempered HAp suspension.

Table 3. Freeze Foaming pressure values characterizing the foaming behavior. [2]

Suspension's Temperature (°C)	Pressure at Beginning of Foaming (mbar)	Pressure at Maximum Foaming Rate (mbar)	Pressure at end of Foaming (mbar)
5	500	40–60	10
40	400	80–100	60

[2] Based on four suspension/Freeze Foams each.

Corresponding to Table 3, Figure 6 also clearly shows that the foaming of 40 °C tempered suspensions finishes earlier when compared to 5 °C foamed suspensions (60 vs. 10 mbar). Additionally, it takes place at a much higher rate (0.045 1/s). Suspensions foamed at 40 °C already reach their maximum after 30 s (at 80–100 mbar), whereas suspensions foamed at 5 °C reach their maximum—continuously foaming—after only 70 s (at 40–60 mbar). The reason for the fast kinetics of the 40 °C suspension foaming is the increased water vapor partial pressure due to the higher temperature as well as the lower viscosity. The 5 °C foamed suspensions reach their maximum foaming rate at a low applied pressure due to the higher viscosity and lower water vapor partial pressure (and therefore a lower driving force).

3.2. Foam Cell Analyses via CT Evaluation

As detailed at the end of Section 2, the green foams were analyzed via CT at the TUD-ILK and later evaluated with VGStudio Max v3.0 to visualize and quantify pore morphology data of scanned foams.

3.2.1. Defect Analyses

The results of the defect analysis are summarized in Tables 4 and 5. The ROI of obtained Freeze Foams covers approximately 95% (5 °C foamed) and 87% (40 °C foamed), respectively, of the overall foam volume. Therefore, it represents the foam volume well. The calculated mean porosity of 5 °C foamed structures (Table 4, 53%) is 5% higher than 40 °C foamed samples (Table 5, 48%). This correlates with the higher foaming degree of 5 °C observed in Section 3.1 (Figure 6). In comparison with the geometrical porosities of Table 2, the defect analyses-derived porosity is lower. This difference is due to the limitation in CT resolution: micropores were not detected.

Table 4. Defect analyses of 5 °C foamed structures. [3]

	5 °C_1	5 °C_2	5 °C_3	5 °C_4	Mean	SD
V_{foam} (mm^3)	2312.41	2449.55	2371.95	2507.32	2410	86
V_{ROI} (mm^3)	2152.95	2350.73	2256.80	2402.62	2291	110
V_{mater} (mm^3)	1021.58	1084.46	1091.48	1148.10	1086	52
V_{def} (mm^3)	1131.37	1266.27	1165.32	1254.52	1204	66
Porosity (%)	52.6	53.9	51.6	52.2	53	0,9
V_{max} (mm^3)	1125.67	1259.81	1159.93	1247.70	1198	66
N	5430	6587	4826	6944	5947	988
V_{max}/V_{def} (%)	99.5	99.5	99.5	99.5	99.5	0.03

[3] V_{foam}: Geometrically measured volume of Freeze Foams, V_{ROI}: Volume of the defined ROIs, V_{mater}: Total volume of material, V_{def}: Total defect volume (i.e., total foam cell volume), V_{max}: Maximum defect volume, N: Number of detected defects.

Table 5. Defect analyses of 40 °C foamed structures. [3]

	40 °C_1	40 °C_2	40 °C_3	40 °C_4	Mean	SD
V_{foam} (mm^3)	1836.89	1800.82	1757.04	1884.67	1820	54
V_{ROI} (mm^3)	1385.70	1652.22	1614.18	1641.88	1573	126
V_{mater} (mm^3)	667.69	868.11	834.18	917.66	822	108
V_{def} (mm^3)	718.01	784.11	780.00	724.22	752	35
Porosity (%)	51.8	47.5	48.3	44.1	48	3,2
V_{max} (mm^3)	714.44	778.63	775.63	719.37	747	35
N	6006	7177	6162	5715	6265	636
V_{max}/V_{def} (%)	99.5	99.3	99.4	99.3	99.4	0.09

[3] V_{foam}: Geometrically measured volume of Freeze Foams, V_{ROI}: Volume of the defined ROIs, V_{mater}: Total volume of material, V_{def}: Total defect volume (i.e., total foam cell volume), V_{max}: Maximum defect volume, N: Number of detected defects.

With regard to the level of interconnectivity, 5 °C as well as 40 °C foamed structures are interconnected to 99% (Table 4, V_{max}/V_{def} (%)). However, this result is not representative of the permeability of the Freeze Foams because neither the average number of connections to neighboring cells nor the cell window size was determined by VGStudio Max.

3.2.2. Foam Structure Analyses

As mentioned in Section 2.1, the segmentation threshold for foam structure analysis was adjusted to be as correct as possible. Figure 7 shows the segmented foam cells. For 5 °C foamed structures it was adjusted to 50% (Figure 7A,C) and for 40 °C foamed structures to 95% (Figure 7B,D). The threshold increase for the 40 °C foamed structures was necessary because their very irregular foam cells would have been segmented otherwise.

Figure 8 shows the results of the foam structure analysis exerted on the struts. Highlighted in rainbow colors are the struts of the 5 °C foamed structures (Figure 8A,C) and the 40 °C foamed structures (Figure 8B,D). Thin struts are marked in blue, with thicker struts in yellow to red. Quantitative data are represented in Figure 9 (right-hand side) and Table 6.

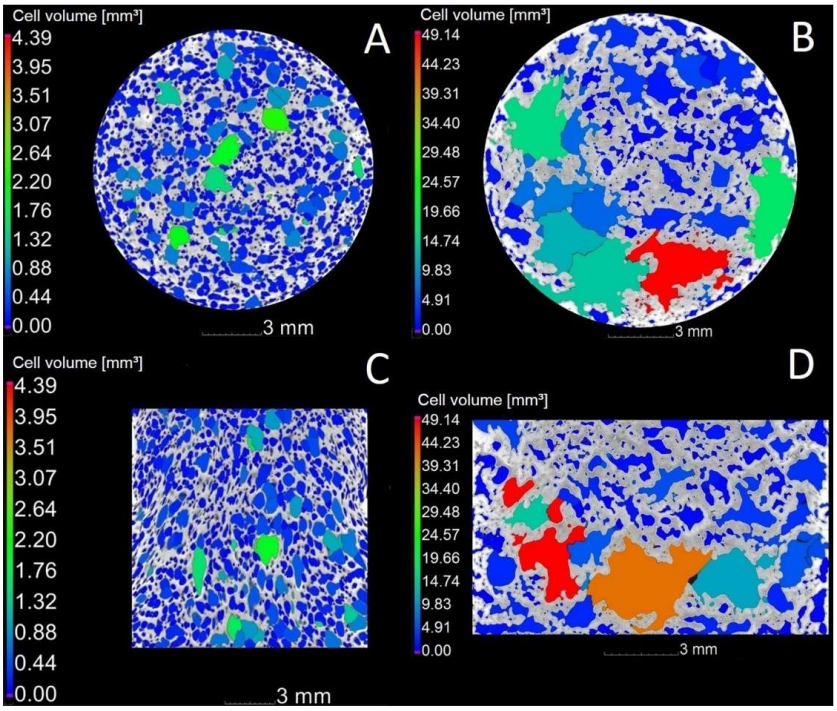

Figure 7. Foam cell segmentation by foam structure analysis module of VGStudio Max 3.0 on the example of *z*-plane (**A**,**B**) and *x*-plane (**C**,**D**) slice images of 5 °C (**A**,**C**) and 40 °C (**B**,**D**) foamed structures. Slices are taken from the middle of the foam volume. Segmentation threshold for 5 °C foams is 50% and for 40 °C 95%.

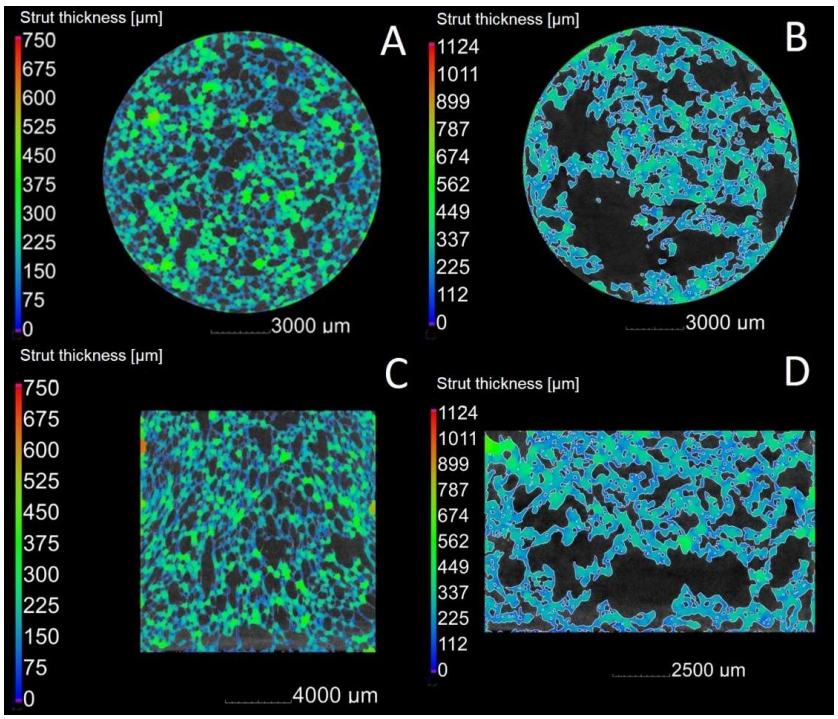

Figure 8. Strut thickness calculated by foam structure analysis module of VGStudio Max 3.0 on the example of *z*-plane (**A**,**B**) and *x*-plane (**C**,**D**) slice images of 5 °C (**A**,**C**) and 40 °C (**B**,**D**) foamed structures. Slices are taken from the middle of the foam volume.

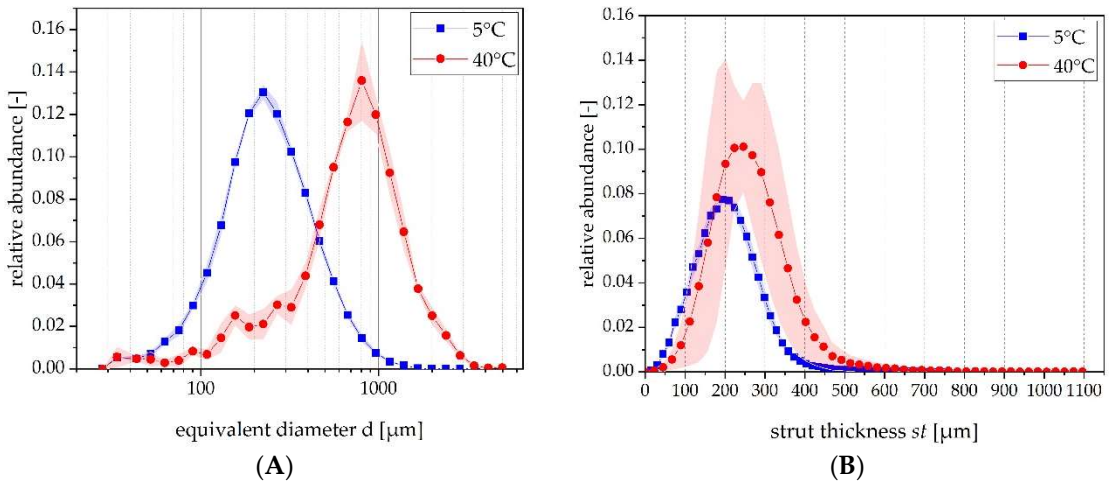

Figure 9. Pore size distribution (**A**) and distribution of strut thickness (**B**) of 5 °C and 40 °C foamed scaffolds (derived from four foams each).

Table 6. Foam structure analyses-derived d_{median} and st_{mean} of 5 °C and 40 °C foamed Freeze Foams.

Sample	d_{median} (µm)	Mean (µm)	SD (µm)	st_{mean} (µm)	Mean (µm)	SD (µm)
5 °C_1	226	231	5	219	215	6
5 °C_2	230			208		
5 °C_3	236			221		
5 °C_4	234			212		
40 °C_1	724	728	43	257	269	10
40 °C_2	711			281		
40 °C_3	789			266		
40 °C_4	690			271		

Figure 9 details the pore size distribution (left) and strut thickness distribution (right) of the obtained Freeze Foams. With regard to the pore size distribution, the 5 °C Freeze Foams feature a monomodal distribution with a maximum peak around 230 µm. The 40 °C Freeze Foams likewise feature a mainly monomodal distribution with the main peak around 800 µm and a small peak at around 160 µm. The large foam cells are suggested to have formed by strong coalescence; the small pores probably represent only slightly coalesced foam cells. In general, 40 °C foamed structures exhibit much wider distribution with small pores (30–200 µm). They are less in abundance compared to the 5 °C foamed Foams, because destabilizing effects (e.g., coalescence and Ostwald ripening) cause them to become larger during the foaming. This behavior is due to the lower viscosity of the suspension (see Figure 5). The width of both progressions furthermore indicates a certain heterogeneity in pore morphology, which is higher when foaming at 40 °C.

With regard to the strut thickness distribution, the 5 °C Freeze Foams feature a slightly narrower distribution than the 40 °C foams. For 40 °C foams, the standard deviation of the relative abundance is much higher, which indicates that the foam structure is less reproducible than that of 5 °C foams. Nevertheless, it can be stated that the strut thickness in 5 °C foams is slightly thinner.

Table 6 shows the resulting mean value of the median equivalent diameter d_{median} and the strut thickness st_{mean}. Obviously, foaming 5 °C tempered suspensions results in much smaller pores than foaming 40 °C tempered suspensions. Therefore, we assess the initial temperature at the beginning of the Freeze Foaming as a crucial influencing factor for the mean value d_{median}. In addition, 40 °C foamed samples show a higher standard deviation, which correlates with a lower reproducibility tendency (see Table 2). With regard to the strut thickness, there are only minor differences between the

two foams compared to the differences in pore size. The thinner struts of 5 °C foams (215 vs. 269 µm) correlate with the higher porosity value (see Tables 4 and 5).

3.2.3. Direction-Dependent Foam Cell Volume Analyses

Figures 10 and 11 show the graphical analyses of 5 and 40 °C foamed suspensions. The variation in progression shows heterogeneity in both sets of Freeze Foams (four cellular structures each). The slice images show individual foam morphologies at particular foam height z in the foaming direction and perpendicular to the foaming direction. Small pores correspond to blue, large pores to red. The averaged foam cell volume is based on three-dimensional calculation, as detailed in Section 2. Figure 10 showcases the specific Freeze Foam "5 °C_1" and Figure 11 the Freeze Foam "40 °C_3". In the foaming direction (analyzed from bottom to top), 5 °C foamed structures show a certain variability of foam cell volume V_{fc} and, therefore, inhomogeneity. It is obvious that the bottom section features larger foam cells (around z = 2–5) than the top (around z = 10–14) (Figure 10A). We suggest two reasons: one is the faster drying at the top compared to the bottom and the second is faster freezing at the top compared to the bottom. In both cases the semi-liquid suspension inhibits bubble growth by drying out and/or freezing. Perpendicular to the foaming (Figure 10B), one side mainly features large foam cells, suggesting border effects, probably due to the high viscosity of the 5 °C tempered suspensions resulting in air pockets during the filling procedure.

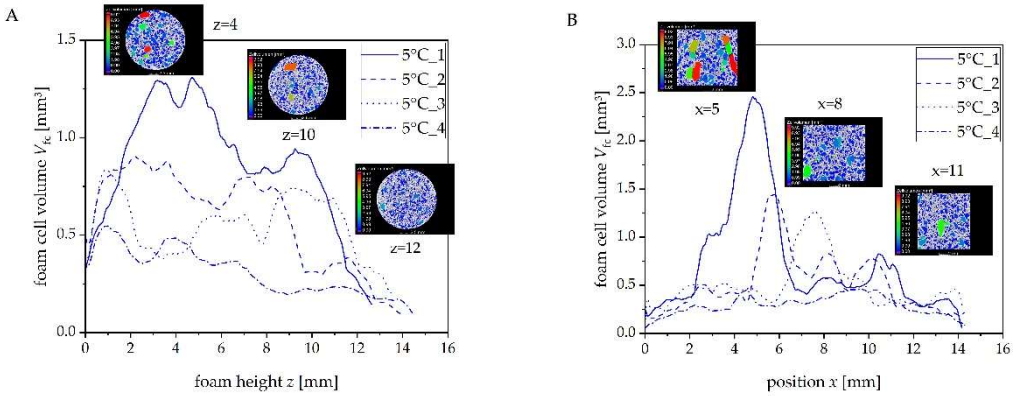

Figure 10. Location-dependent foam cell volume V_{fc} of 5 °C foamed suspension (**A**) foaming direction analyzes; (**B**) perpendicular to foaming direction.

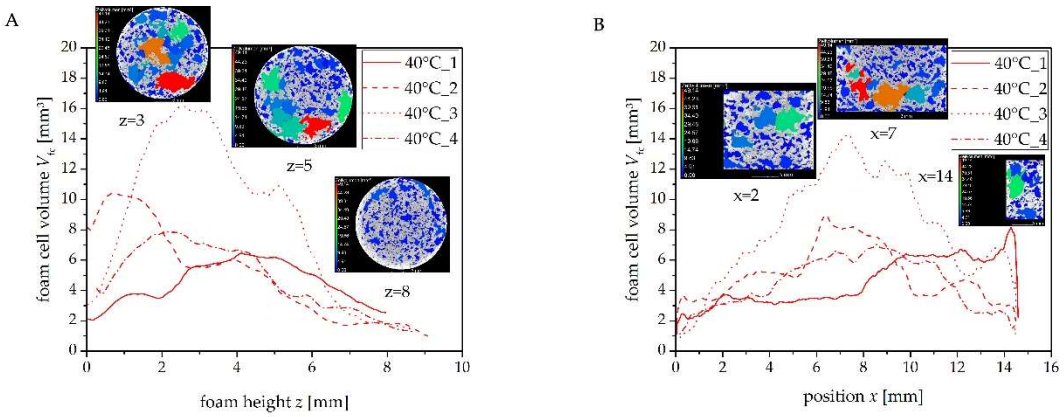

Figure 11. Location-dependent foam cell volume V_{fc} of 40 °C foamed suspension: (**A**) foaming direction analyses; (**B**) perpendicular to foaming direction.

Observing the 40 °C foamed structures (Figure 11A), similar to the 5 °C foams, a majority of large pores becomes obvious within the bottom section of the selected Freeze Foams in the direction

of foaming (Figure 11A). Perpendicular to the foaming direction large pores are mainly found in the center of selected Freeze Foams (Figure 11B).

By determining the location-dependent foam cell's volume $V_{fc}(z)$ in the corresponding foaming plane we were able to calculate V_{fca}, the specific arithmetic Freeze Foam cell's average value (Equation (4); Figure 4). A high V_{fca} corresponds to a large variability in foam cell volume—a heterogeneous foam structure; a low V_{fca} corresponds to a more homogeneous pore morphology.

Tables 7 and 8 summarize the calculated values for Freeze Foams foamed at 5 °C and 40 °C, respectively. By comparing the average V_{fca} in both analysis directions and in accordance with Figures 7 and 8, we observe that 5 °C foams result in much more homogeneous structures than 40 °C foams. Furthermore, in accordance with Figure 10A,B, 5 °C foamed Freeze Foams are more homogeneous in the direction of the foaming than perpendicular to it (Table 7, $V_{fca\_average}$ = 0.19 vs. 0.37). However, these findings need to be regarded critically because the SD constitutes approximately 50% of the mean value. This deviation is likely the result of the filling procedure, which causes boundary effects (as stated before) and is not due to the process itself.

Table 7. Arithmetic foam cell's volume of Freeze Foams foamed at 5 °C.

Sample		V_{fca} 5 °C_1	5 °C_2	5 °C_3	5 °C_4	$V_{fca\_average}$	SD_{Vfca}
Analyses direction	Foaming direction	0.28	0.24	0.13	0.10	0.19	0.09
	Perpendicular to foaming direction	0.73	0.37	0.31	0.08	0.37	0.27

Table 8. Arithmetic foam cell's volume of Freeze Foams foamed at 40 °C.

Sample		V_{fca} 40 °C_1	40 °C_2	40 °C_3	40 °C_4	$V_{fca\_average}$	SD_{Vfca}
Analyses direction	Foaming direction	1.17	2.57	4.55	1.95	2.56	1.44
	Perpendicular to foaming direction	1.48	1.38	3.01	1.56	1.86	0.77

In contrast to 5 °C foamed structures, 40 °C Freeze Foams are less homogeneous when considered in the direction of foaming (Table 8, $V_{fca\_average}$ = 2.56 vs. 1.86). The abovementioned tendency of faster drying out and freezing at the top section of foams is more prominent because of an increased water vapor partial pressure leading to increased water evaporation. Lower viscosity results in less disturbing boundary effects (air pockets due to filling).

We assess the new findings, i.e., 5 °C Freeze Foams being more homogeneous than 40 °C Freeze Foams, as adequately proven by our CT evaluations.

3.3. Microstructure Analyses of Obtained Freeze Foams

For evaluating the micropores of obtained HAp Freeze Foams, SEM analyses were conducted. Figures 12 and 13 display the fracture analyses and ion-polished microstructure analyses, respectively, of the cellular structures foamed at 5 °C.

With regard to Figure 12, a mix of different pore sizes (100–600 µm) can be observed. The Freeze Foam's struts are filled and highly microporous. The side view shows the foam cell's orientation in the direction of the foaming (bottom to top). Also, the cell walls feature microporosity. These small pores reflect the cryogenic texture, which is the residue of sublimated ice crystals (process induced as stated in Section 1).

The microstructural images in Figure 13 also present a mix of different pore sizes. These lie between 100 and 2000 µm and vary between spherical and elongated shape. Due to the low suspension temperature, foam destabilizing effects like Ostwald ripening, coalescence or drainage were kept to a minimum, although some pores already show a beginning coalescence. The microporous struts exhibit some denser regions. Possible reasons may be: inhomogeneous distribution of water in cell walls or

(visualizing a 3D volumetric view), existing neighboring struts where parts are denser, and neighboring cells where struts are more porous.

Figures 14 and 15 display the fracture analyses and ion-polished microstructure analyses, respectively, of the cellular structures foamed at 40 °C. In contrast to the images above, the Freeze Foam is highly heterogeneous in structure. Large voids rather than well-shaped pores are connected by thick and microporous filled struts. Again, cryogenic texture along the cell walls can be observed. The microstructural images (Figure 15) only show a few small pores in the region of 200 µm. The majority are large voids or irregular shaped pores. Like the Freeze Foams obtained from a 5 °C tempered suspension, the 40 °C foamed Freeze Foam's microporous struts also show denser and more porous regions, likely being subject to the same occurrences mentioned above.

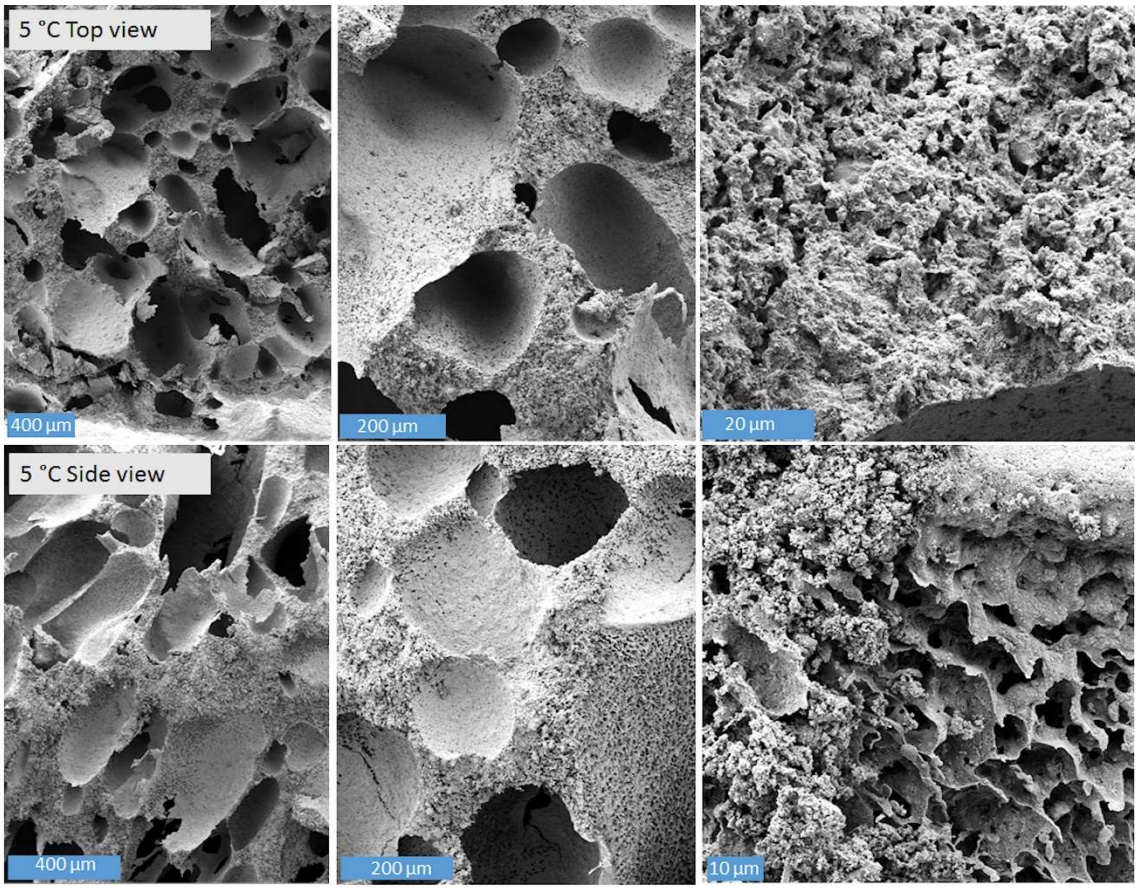

Figure 12. Fracture SEM images of HAp Freeze Foams foamed at 5 °C.

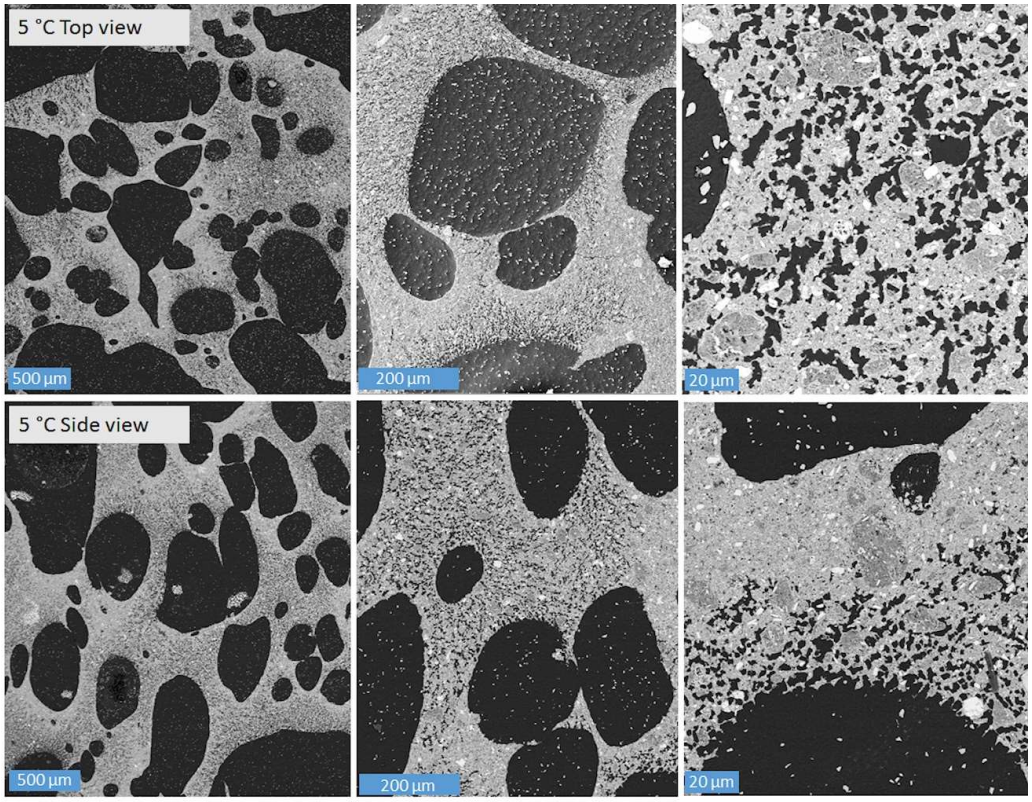

Figure 13. Microstructural SEM images of HAp Freeze Foams foamed at 5 °C.

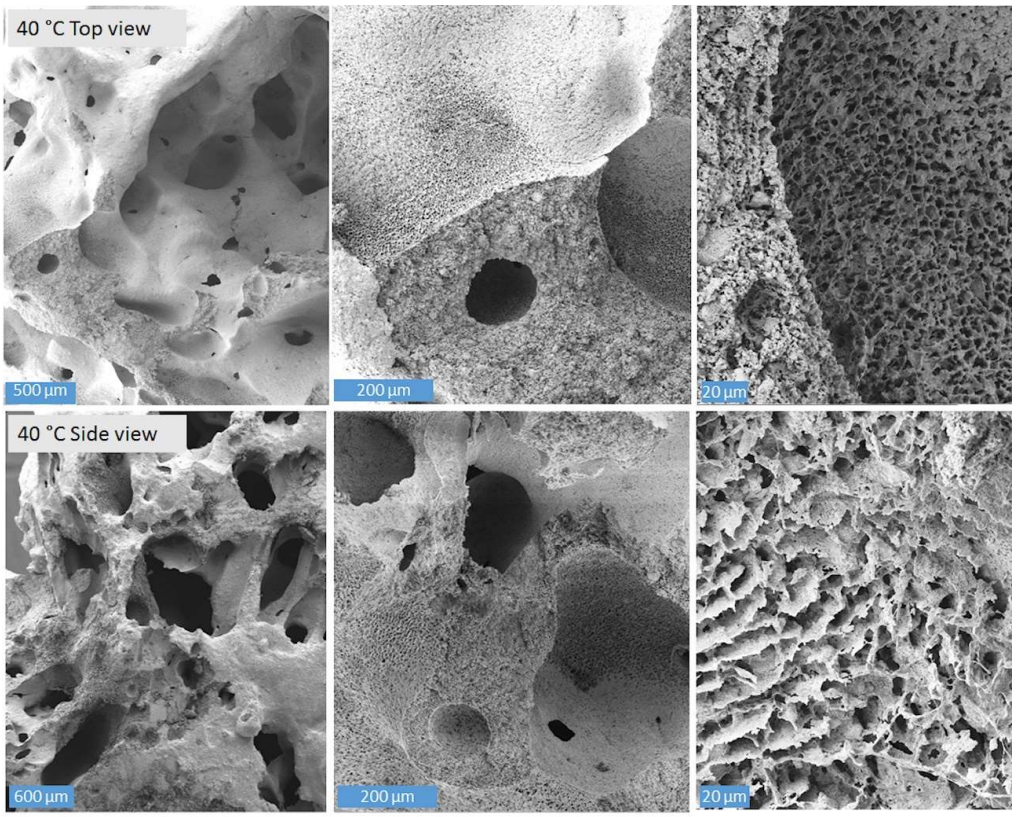

Figure 14. Fracture SEM images of HAp Freeze Foams foamed at 40 °C.

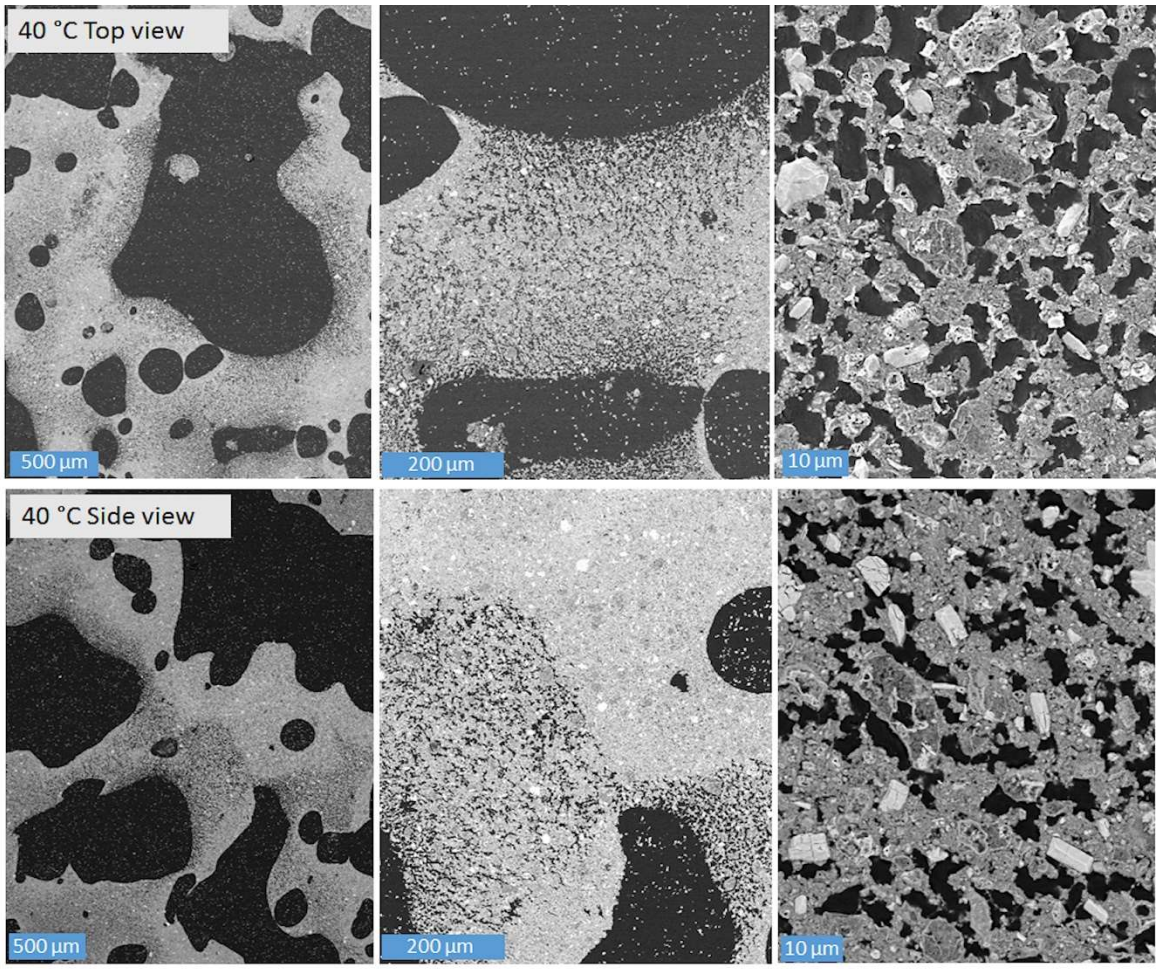

Figure 15. Microstructural SEM images of HAp Freeze Foams foamed at 40 °C.

4. Conclusions and Outlook

We succeeded in manufacturing reproducible Freeze Foams (by geometrical porosity) that appear stable when foamed with 5 and 40 °C tempered suspensions. CT-derived quantitative analyses of the pore morphology as well as SEM images show that pore size, shape and distribution are not reproducible and vary significantly at this stage. Proven by the newly introduced specific arithmetic Freeze Foam cell's average parameter V_{fca}, this especially applies with regard to cellular Freeze Foams foamed at 40 °C. Nevertheless, the presented findings strongly indicate that the foaming of 5 °C tempered suspensions might lead to homogeneous pore morphology. One of the main findings of the first period was that Freeze Foam's pores are becoming larger and more irregular the faster the pressure reduction rate [9]. Therefore, with regard to the aim of achieving a homogeneous pore structure, we now identify the temperature and the pressure reduction rate as significant process parameters that have to be controlled. In follow-up research we will combine these factors and evaluate their effect on the foam's structure.

We also identified specific main regions of foaming activity by calculating the foaming degree and rate. Follow-up research will deal with targeted foaming control by deliberately adding pressure holds within these regions.

Mold-related issues (geometry, material) and the filling procedure (the possibility of enclosed air in the suspension) will be further points of interest since they have an effect on the pore structure of obtained Freeze Foams and have to be minimized. In that regard, so far we cannot transfer the exact findings/principles of this contribution to the manufacturing of larger structures. However,

considering and systematically combining all of these found adjusting screws, we are getting closer to reproducible and homogeneous pore morphologies manufactured via Freeze Foaming.

As stated in Section 1, this contribution mainly reports on green-state Freeze Foams. This is useful and necessary in terms of evaluating how suspension and foaming process affect the resulting pore structure. Sintered foams, though, will play a role in applications and, therefore, are subject to subsequent analyses and comparison to their green-state condition.

Author Contributions: M.A. is the DFG-funded project's editor and manager, scientifically conceiving, guiding and supervising experiments and evaluations as well as writing the manuscript; project editor D.W. mainly is working on the scientifically relevant questions concerning the experiments and significantly contributed to the evaluations and analyses; N.K. and J.A., both project editors, worked on the numerous experiments presented in this contribution; J.M. and T.B. are the DFG project's manager and editor from the TU-DD ILK; T.M., A.M., and M.G. helped with higher-ranked issues and questions.

Funding: This work has been funded by DFG (Grant number 310892168) and the Fraunhofer Society.

Acknowledgments: The authors very much appreciate the support and assistance of David Werner and Nils Kaube, as well as the project partner's TUD-ILK assistance, work and many enlightening hours together.

Conflicts of Interest: The authors declare no conflict of interest. The founding sponsors had no role in the design of the study; in the collection, analyses, or interpretation of data; in the writing of the manuscript, and in the decision to publish the results.

References

1. Du Pont de Nemours, E.I. Colloidal Silica Foam. UK Patent 1175760, 21 December 1967.
2. Wood, L.; Messina, P.; Frisch, C. Method of Preparing Porous Ceramic Structures by Firing a Poplyurethane Foam that Is Impregnated with Inorganic Material. U.S. Patent 3833386, 3 September 1974.
3. Eckert, K.-L.; Mathey, M.; Mayer, J.; Homberger, F.; Thomann, P.; Groscurth, P.; Wintermantel, E. Preparation and in vivo testing of porous alumina ceramics for cell carrier applications. *Biomaterials* **2000**, *21*, 63–69. [CrossRef]
4. Schwartzwalder, K.; Somers, A. Method of Making Porous Ceramics Articles. U.S. Patent 3090094, 21 May 1963.
5. Komarneni, S.; Pach, L.; Pidugu, R. Porous α-alumina ceramics using bohemite and rice flour. *Mater. Res. Soc. Symp. Proc.* **1995**, *371*, 285–290.
6. Lopes, R.A.; Segadaes, A.M. Microstructure, permeability and mechanical behavior of ceramic foams. *Mater. Sci. Eng.* **1996**, *209*, 149–155. [CrossRef]
7. Moritz, T. Lightweight Green Compact and Molded Article Made of a Ceramic and/or Powder-Metallurgical Material, and the Method for the Production of Thereof. Patent DE102008000100, 18 January 2008.
8. Ahlhelm, M. *Gefrierschäume—Entwicklung von Zellularen Strukturen für Vielfältige Anwendungen/Freeze Foams—Development of Cellular Structures for Various Applications*; Schriftenreihe Kompetenzen in Keramik; Fraunhofer, I.K.T.S., Alexander, M., Eds.; Fraunhofer Verlag: Dresden, Germany, 2016; Band 32; ISBN 978-3-8396-0977-4.
9. Ahlhelm, M.; Werner, D.; Maier, J.; Abel, J.; Behnisch, T.; Moritz, T.; Michaelis, A.; Gude, M. Evaluation of the pore morphology formation of the Freeze Foaming process by in situ computed tomography. *J. Eur. Cerm. Soc.* **2018**, *38*, 3369–3378. [CrossRef]
10. Deville, S.; Saiz, E.; Tomsia, A.P. Freeze casting of hydroxyapatite scaffolds for bone tissue engineering. *Biomaterials* **2006**, *27*, 5480–5489. [CrossRef] [PubMed]
11. Deville, S. Freeze-Casting of Porous Biomaterials: Structure, Properties and Opportunities. *Materials* **2010**, *3*, 1913–1927. [CrossRef]
12. Ahlhelm, M.; Fruhstorfer, J.; Moritz, T.; Michaelis, A. The Manufacturing of Lightweight Refractories by Direct Freeze Foaming Technique. *Interceram* **2011**, *60*, 394–399.
13. Ahlhelm, M.; Moritz, T. Synthetic Bone Substitute Material and Method for Producing the Same. European Patent EP2682137A3, 1 February 2013.
14. Ahlhelm, M.; Moritz, T. Herstellung eines biokompatiblen Hydroxylapatit-ZrO_2-Hybridschaums über die Methode der Gefrier-Direktschäumung. In *Schriftenreihe Werkstoffe und Werkstofftechnische Anwendungen*; Wielage, B., Ed.; Deutsche Gesellschaft für Materialkunde e.V. DGM: Chemnitz, Gemany, 2011; Volume 41.

15. Ahlhelm, M.; Gorjup, E.; von Briesen, H.; Moritz, T.; Michaelis, A. Freeze-foaming-a promising approach to manufacture strength enhanced ceramic cellular structures allowing the ingrowth and differentiation of human mesenchymal stem cells. In Proceedings of the International Conference MiMe-Materials in Medicine (1st edition MIME), Faenza, Italy, 8–11 October 2013.
16. Ahlhelm, M.; Günther, P.; Scheithauer, U.; Schwarzer, E.; Günther, A.; Slawik, T.; Moritz, T.; Michaelis, A. Innovative and novel manufacturing methods of ceramics and metal-ceramic composites for biomedical applications. *J. Eur. Cerm. Soc.* **2016**, *12*, 2883–2888. [CrossRef]
17. Ahlhelm, M.; Schwarzer, E.; Scheithauer, U.; Moritz, T.; Michaelis, A. Novel ceramic composites for personalized 3D-structures. *J. Ceram. Sci. Technol.* **2017**, *8*, 91–100.
18. Routschka, G. *Feuerfeste Werkstoffe*; Vulkan-Verlag: Essen, Gemany, 1997; p. 2.
19. Sepulveda, P.; Bressiani, A.H.; Bressiani, J.C.; Meseguer, L.; König, B., Jr. In vivo evaluation of hydroxyapatite foams. *J. Biomed. Mater. Res.* **2002**, *62*, 587–592. [CrossRef] [PubMed]
20. Rueger, J.M.; Linhart, W.; Sommerfeldt, D. Biologische Reaktionen auf Kalziumphosphatkeramik-Implantationen. Tierexperimentelle Ergebnisse. In *Der Orthopäde*; Springer-Verlag: Berlin/Heidelberg, Germany, 1998; Volume 27, pp. 89–95.
21. Best, S.M.; Porter, A.E.; Thiana, E.S.; Huang, J. Bioceramics: Past, present and for the future. *J. Eur. Cerm. Soc.* **2008**, *28*, 1319–1327. [CrossRef]
22. Hutmacher, D.W. Scaffolds in tissue engineering bone and cartilage. *Biomaterials* **2000**, *21*, 2529–2543. [CrossRef]
23. Karageorgiou, V.; Kaplan, D. Porosity of 3D biomaterial scaffolds and osteogenesis. *Biomaterials* **2005**, *26*, 5474–5491. [CrossRef] [PubMed]
24. Wegst, U.G.K. Biomaterials by freeze casting. *Philos. Trans. R. Soc. A* **2010**, *368*, 2099–2121. [CrossRef] [PubMed]
25. Nakayama, H. Nondestructive Microstructural Analysis of Porous Bioceramics by Microfocus X-ray Computed Tomography (μCT): A Proposed Protocol for Standardized Evaluation of Porosity and Interconnectivity Between Macro-pores. *J. Nondestruct. Eval.* **2011**, *30*, 71–80. [CrossRef]
26. Peyrin, F. Evaluation of bone scaffolds by micro-CT. *Osteoporos. Int.* **2011**, *22*, 2043–2048. [CrossRef] [PubMed]
27. Jones, J.R.; Poologasundarampillai, G.; Atwood, R.C.; Bernard, D.; Lee, P.D. Non-destructive quantitative 3D analysis for the optimisation of tissue scaffolds. *Biomaterials* **2007**, *28*, 1404–1413. [CrossRef] [PubMed]
28. Van Lenthe, G.H.; Hagenmüller, H.; Bohner, M.; Hollister, S.J.; Meinel, L.; Müller, R. Nondestructive micro-computed tomography for biological imaging and quantification of scaffold–bone interaction in vivo. *Biomaterials* **2007**, *28*, 2479–2490. [CrossRef] [PubMed]
29. Ducheyne, P.; Qiu, Q. Bioactive ceramics: The effect of surface reactivity on bone formation and bone cell function. *Biomaterials* **1999**, *20*, 2287–2303. [CrossRef]
30. Shors, E.C.; Holmes, R.E. Porous hydroxyapatite. In *An Introduction to Bioceramics. Advanced Series in Ceramics*; Hench, L.L., Wilson, J., Eds.; World Scientific Publishing Co.: Singapore, 1993; Volume 1, pp. 181–198.
31. Liu, D.M. Porous hydroxyapatite bioceramics. In *Key engineering Materials*; Liu, D.M., Ed.; Trans Tech Publications: Uetikon-Zurich, Switzerland, 1996; Volume 115, pp. 209–232.
32. VGSTUDIO. Available online: https://www.volumegraphics.com/de/produkte/vgstudio.html (accessed on 2 May 2018).
33. DIN EN ISO 4287. *Geometrical Product Specifications (GPS)—Surface Texture: Profile Method—Terms, definitions and surface texture parameters (ISO 4287:1997 + Cor 1:1998 + Cor 2:2005 + Amd 1:2009)*; International Organization for Standardization: Geneva, Switzerland, 1997; pp. 1–24.